RESEARCH ARTICLE
SPACE PHYSICS

Earth and Planetary Physics
10: 105–116, 2026
doi: 10.26464/epp2026003

Global thermospheric density response to the May 2024 extreme storm: TianMu-1 constellation observations

JiangZhao Ai[1,2,3], XianGuo Zhang[1,2,3*], YongPing Li[1,2,3*], YueQiang Sun[1,2,3], WenLu Bai[4], XiaoYu Guo[4], JiaoJiao Zhang[1], XiaoLiang Zheng[1,2,3], Jia Li[1,2], YuJie Wang[1,2], and XinChun Tang[5]

[1]National Space Science Center, Chinese Academy of Sciences, Beijing 100190, China;

[2]Beijing Key Laboratory of Space Environment Exploration, Beijing 100190, China;

[3]University of Chinese Academy of Sciences, Beijing 100049, China;

[4]Aerospace Tianmu (Chongqing) Satellite Science & Technology Co., Ltd., Chongqing 401332, China;

[5]Shenzhen Aerospace Dongfanghong Satellite, Ltd., Shenzhen 518057, China

Key Points:

- After deployment, TianMu-1's first concurrent multiple local time (LT) observation captured the May 2024 superstorm using five satellites.
- We quantified the LT dependence of thermospheric hemispheric asymmetry driven by the May 2024 superstorm based on multisatellite synchronous observations.
- We directly resolved the entire evolutionary sequence of global multi-LT traveling atmospheric disturbances, from generation through propagation to dissipation, including their LT-dependent modulation.

Citation: Ai, J. Z., Zhang, X. G., Li, Y. P., Sun, Y. Q., Bai, W. L., Guo, X. Y., Zhang, J. J., Zheng, X. L., Li, J., Wang, Y. J., and Tang, X. C. (2026). Global thermospheric density response to the May 2024 extreme storm: TianMu-1 constellation observations. *Earth Planet. Phys.*, *10*(1), 105–116. http://doi.org/10.26464/epp2026003

Abstract: In this study, we analyze the impact of the May 2024 geomagnetic storm on the thermospheric mass density by using TianMu-1 constellation satellite (TM02, TM06, TM07, TM11, TM15) observations. These observations reveal intense large-scale traveling atmospheric disturbances (TADs) originating at high latitudes and propagating equatorward. Observations by TM02 captured the evolution of a TAD structure: An initial amplitude of ~3.89×10^{-12} kg/m^3 at hundred-kilometer scale subsequently intensified to 4.78×10^{-12} kg/m^3, with the spatial extent expanding to the thousand-kilometer level. Significant hemispheric asymmetry was observed: the absolute density was higher predominantly in the northern hemisphere (TM02, TM06, TM07, TM11), whereas the difference in the relative density consistently showed greater enhancements in the southern hemisphere across all satellites, with the maximum north–south density differences exceeding 195%–640% above 60° latitude. In conjunction with SuperDARN (Super Dual Auroral Radar Network) observations, this striking hemispheric asymmetry can likely be attributed to disparities in plasma convection patterns between the two hemispheres. Furthermore, density perturbation characteristics exhibited strong local time (LT) dependence: Near noon (~10.7 LT, TM02 descending), the northern hemisphere onset preceded the southern onset. Conversely, near dusk (~17.6 LT, TM15 descending), the southern onset led the northern onset by approximately 3 hours. Ascending orbits (TM02, TM06, TM07, TM15) typically yielded larger global density enhancements compared with smaller southern-confined enhancements during descending orbits. Satellite TM11 showed comparable perturbations in both ascending and descending orbits. By leveraging its unique orbital architecture, the TianMu-1 constellation enables global near-simultaneous multi-LT sampling, providing a robust data foundation for both scientific research and engineering applications.

Keywords: TianMu-1 constellation; thermosphere density; magnetic storm; hemispheric asymmetry; traveling atmospheric disturbances

1. Introduction

The thermosphere, the uppermost layer of Earth's atmosphere extending from approximately 80 km to thousands of kilometers, plays a crucial role in the dynamics and energetics of the upper atmosphere (Powell, 2018). It undergoes significant variations in its density and composition as a result of various space weather phenomena, particularly geomagnetic storms, which are intense disturbances in Earth's magnetic field caused by solar wind interactions with the magnetosphere. Geomagnetic storms are driven by solar wind plasma, particularly during periods of coronal mass ejections and high-speed solar wind streams (Denton et al., 2006).

First author: J. Z. Ai, aijiangzhao@nssc.ac.cn
Correspondence to: X. G. Zhang, zhangxg@nssc.ac.cn
Y. P. Li, lyp@nssc.ac.cn
Received 15 JUN 2025; Accepted 08 SEP 2025.
First Published online 24 SEP 2025.

These phenomena can substantially compress and distort Earth's magnetosphere, leading to enhanced currents in the ionosphere and thermosphere (Sarris, 2019). These currents, in turn, deposit energy into the upper atmosphere through Joule heating and particle precipitation, causing substantial changes in thermospheric density and neutral compositions (Richards et al., 2013). Cai L et al. (2014) showed that Joule heating can account for the vast majority of energy injected into the thermosphere at high latitudes during geomagnetic storms, which leads to a sharp increase in the density of the thermospheric atmosphere. In addition, Wang X et al. (2020) conducted a statistical analysis of Joule heating versus different levels of geomagnetic storms based on densities obtained by the Challenge Microsatellite Payload (CHAMP) and the Gravity Recovery and Climate Experiment (GRACE). The analytic results showed that the peak duration of Joule heating is positively correlated with the intensity of geomagnetic storms. Zhang B et al. (2012) confirmed by running a coupled magnetosphere–ionosphere–thermosphere (CMIT) model that the increase in density at high latitudes is associated with soft electron precipitation. The response of the thermosphere to geomagnetic storms is not limited to density changes. The composition of the atmosphere also undergoes modifications as high-energy particles from the solar wind interact with atmospheric constituents. Cai XG et al. (2023) used Global-scale Observations of Limb and Disk (GOLD) observations to study the response of the thermosphere composition to storms affecting Space-X. The GOLD observations showed that the percentage difference in the O and N_2 column density ratio ($\sum O/N_2$) of between-storm and quiet-time conditions occurs in the depletion zone at middle- and high-latitude levels in the local noon sector of the southern hemisphere. These interactions can also lead to the production of new species, such as nitric oxide (NO), which further affects the atmospheric chemistry and energy balance (Solomon et al., 2007). The resulting changes in the thermosphere can have cascading effects on other atmospheric layers, including the mesosphere and stratosphere, through wave-mean flow interactions and other dynamic processes (Cnossen et al., 2024).

Research into the response of the thermosphere mass density to geomagnetic storms has gained considerable momentum in recent years, driven by advances in space-based observations. Satellites such as CHAMP and GRACE have provided valuable data on atmospheric density variations during geomagnetic storms, enabling researchers to better understand the underlying physical mechanisms (Emmert et al., 2010). These observations have revealed that changes in the thermosphere density can be substantial, with increases of up to several hundred percent compared with quiet-time conditions (Liu H et al., 2014). Previous studies have shown hemispheric asymmetry in the increase in density at high latitudes during geomagnetic storms (Ercha et al., 2012; Li YP et al., 2023, 2024). The analysis of data detected by the Atmospheric Density and Precise Orbit Determination (APOD) satellite during the geomagnetic storm event on September 8, 2017, as reported by Ai JZ et al. (2023), indicated that the amplitude of the density response in the southern polar region was approximately 1.33 to 1.65 times that of the northern polar region. The asymmetry in plasma convection between the hemispheres results in hemispheric variations in Joule heating at high latitudes, serving as a significant factor contributing to the hemispherical discrepancy in the density response during the storm (Xiao C et al., 2023; Zhu QY et al., 2023). Additionally, the hemispheric asymmetry in density enhancements exhibits a correlation with local time (LT) differences. Li RX and Lei JH (2021) studied the GRACE and SWARM satellite data and found that the density enhancement near ~8/20 LTs had hemispheric symmetry, whereas the enhancement was more pronounced in the southern hemisphere in the afternoon region.

Traveling atmospheric disturbances (TADs) are common and important physical phenomena in the thermosphere during magnetic storms that can affect the redistribution of global thermosphere energy, and they have been widely studied by scientific researchers (Fujiwara and Miyoshi, 2006; Bruinsma and Forbes, 2007; England et al., 2021). For example, on the basis of CHAMP satellite accelerometer-derived density data at 400 km altitude, Bruinsma and Forbes (2007, 2009) revealed substantial hemispheric asymmetry in dayside TAD propagation speeds and substantially higher average propagation speeds on the nightside than on the dayside, with neither the TAD amplitude nor phase speed showing a clear correlation with the *Kp* index. Xu S et al. (2021) found that the spatial distribution of high-latitude TADs under magnetostatic conditions showed a significant spatial scale and high dependence based on the southern hemisphere winter observations of Gravity Field and Steady-State Ocean Circulation Explorer (GOCE) and CHAMP satellites at different altitudes. Building on the aforementioned observational studies, Pham et al. (2022) utilized the high-resolution Multiscale Atmosphere Geospace Environment (MAGE) model to simulate TADs during the August 24–25, 2005, geomagnetic storm event. Their simulations further demonstrated that TADs generated at high latitudes propagate equatorward, subsequently inducing global-scale thermospheric density perturbations. Although considerable research has been conducted on TADs, the systematic elucidation of their physical mechanisms—spanning generation, propagation, and dissipation—remains a significant challenge. The TianMu-1 constellation, by leveraging its unique capability for simultaneous multi-LT global observations, promises to provide critical observational support to unravel these mechanisms.

2. Data

2.1 TianMu-1 Constellation

The TianMu-1 constellation has been launched successively beginning in January 2023, with a construction scale of 72 satellites capable of integrated detection of the thermosphere and ionosphere. As of January 2024, the TianMu-1 constellation has launched 23 satellites, of which 12 satellites are equipped with 10 atmospheric density detectors (ADDs) and 2 atmospheric composition detectors (ACDs). The ADDs and ACDs have the function of monitoring *in situ* atmospheric density and atmospheric composition. Table 1 provides the spatial distribution and payload configuration of the 12 *in situ* atmospheric detection satellites.

The 12 TianMu-1 *in situ* atmospheric observation satellites listed in Table 1 are distributed in a sun-synchronous orbit at an inclination of 97° and an altitude of approximately 500 km, and they are

Table 1. Layout and number of satellites in the TianMu-1 constellation, and the payload configuration related to *in situ* atmospheric monitoring.

Launch date	Descending/ascending node local time	Satellite name (s)	Satellite number	Payload[a]
December 25, 2023	07:20/19:20	TM11	1	ADD
July 20, 2023	09:40/21:40	TM07, TM08	2	ADD
January 9, 2023	11:30/23:30	TM01, TM02	2	ADD
December 27, 2023	13:10/01:10	TM19, TM20	2	ACD
March 22, 2023	15:30/03:30	TM03–TM06	4	ADD
January 5, 2024	17:50/05:50	TM15	1	ADD

[a]ADD, atmospheric density detector; ACD, atmospheric composition detector.

evenly distributed in six different orbital planes. The descending/ascending nodes of the six orbital planes are 07:20/19:20 LT, 09:40/21:40 LT, 11:30/23:30 LT, 13:10/01:10 LT, 15:30/03:30 LT, and 17:50/05:50 LT. Except for TM19 and TM20 at 13:10/01:10 LT, which are equipped with ACDs, the remaining 10 satellites are equipped with ADDs. The basic principle of mass density measurement by the ADD instrument is as follows: According to the basic assumption of the ADD instrument design (Qin GT et al., 1990), the gas molecules in the sampling chamber are in a state of equilibrium, meaning that the average mass of atmospheric molecules entering and leaving the sampling chamber is approximately balanced. Under free molecular flow and thermal equilibrium conditions, gas molecules follow the Maxwellian velocity distribution. By integrating the velocity distribution function, the number density outside the sensor can be obtained—which is related to the sampling chamber pressure and sampling chamber temperature. To derive the mass density, the average molecular mass must be known. In the study by Li X et al. (2018), the average molecular mass was derived from the NRLMSISE00 atmospheric density model. In the present work, however, the calculation method of the average molecular mass is determined by using the following method: On the basis of the historical *in situ* measurement data of different orbit types and space environment parameters, a polynomial functional relationship between the average molecular mass and the number density is established. Using this relationship and the number density measured by the ADD instrument, we can calculate the average molecular mass and then obtain the mass density information. According to the processing method above, the on-orbit calibration method for ADD mass density utilizes the atmospheric mass density derived from two-line element (TLE) data as a quasi-true reference value. A linear fit is then applied to calibrate the raw mass density against this reference. The calibrated mass density has a temporal resolution of 1 second with an accuracy better than 7%. The ACD uses a mass analyzer to separate and collect different gas ions after ionization to obtain the density of different neutral components. The ACD has the ability to measure neutral gases with masses in the range of 2–34 amu (atomic mass units), whereas the highly neutral components of the TianMu-1 satellite orbits are predominantly O and N_2. Such satellite layouts and payload configurations are important for understanding the changing characteristics of the neutral atmosphere in the thermosphere.

The atmospheric density data studied in this work are derived from ADD instruments in different LT planes to analyze the impact of magnetic storms on the global thermospheric atmosphere, as shown in Figure 1. The colored dots in the diagram show that TM02 and TM06 are close in altitude to approximately 490 to 511 km but approximately 30 km lower than the other three satellites.

2.2 Solar and Geomagnetic Behavior

As solar activity continued to intensify in the days leading up to May 10, a series of coronal mass ejections were ejected from the active region of AR3664, causing an extreme G5 geomagnetic storm to erupt on Earth at approximately 17:00 UTC (Coordinated Universal Time) on May 10, 2024, when the interplanetary magnetic field began to oscillate violently, as shown in Figure 2. The *Kp* index rose directly to 9 after 3 hours and remained above 8 for nearly 33 hours under the continuous pressure of the solar wind. The appearance of such a strong G5 storm dates back 20 years to November 2004. During the entire storm period, the auroral electrojet (*AE*) index exhibited violent fluctuations, peaking at 4098 nT. Meanwhile, the geomagnetic disturbance storm time (*Dst*) index plummeted to −412 nT, nearly 40 nT lower than the minimum *Dst* value recorded during the November 2004 magnetic storm. Consequently, the geomagnetic storm of May 10–12, 2024, is now recognized as the most intense such event recorded since 2004 (Chernogor et al., 2025). Our aim was to determine the response characteristics of the thermospheric atmosphere in such a strong geomagnetic storm.

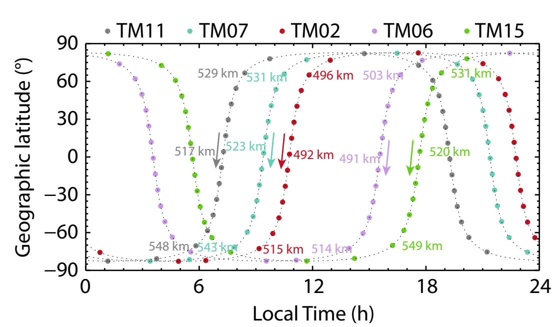

Figure 1. Geographic latitude–local time coverage curves (gray lines) for the TM02, TM06, TM07, TM11, and TM15 satellites from May 10 to 12, 2024. The colored dots represent the spatial positions of the corresponding satellites at a certain time interval, and the altitudes are marked on the map. The arrow points in the direction of the satellite's movement.

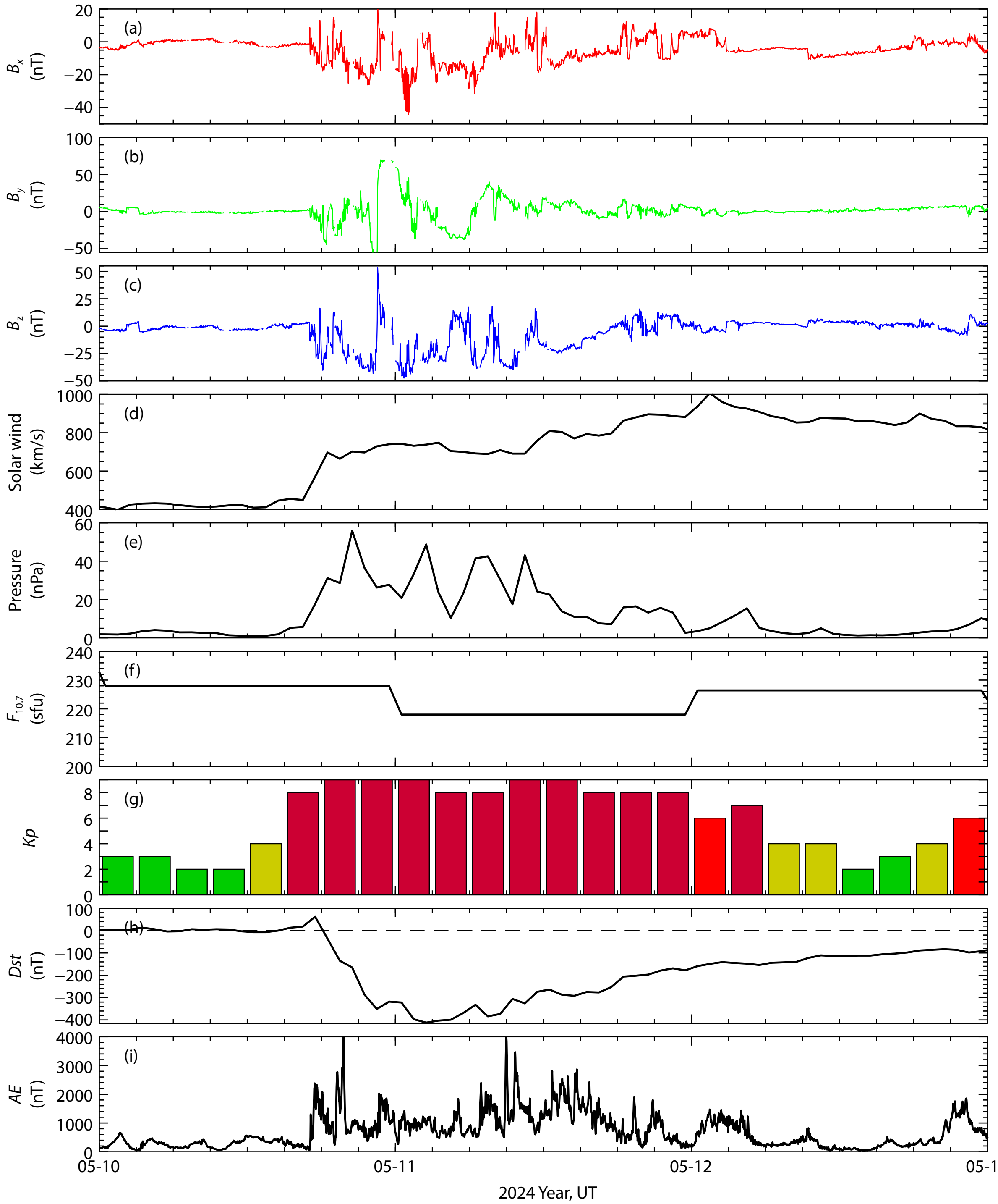

Figure 2. Time series changes in solar and geomagnetic indices for the period of May 10 to 12, 2024. From top to bottom, the interplanetary magnetic field B_x, B_y, B_z, solar wind velocity, dynamic pressure, solar radiation index $F_{10.7}$, and geomagnetic indexes *Kp*, *Dst*, and *AE*.

3. Results

3.1 Mass Density Response

Figure 3 shows the thermospheric mass density observations of five satellites from different orbital planes of the TianMu-1 constellation during the strong geomagnetic storm from May 10 to 12, 2024. During the magnetic storm, the true density observations for each satellite were normalized to the mean altitude indicated in the title of each subplot, as shown in Figures 3a–3j. The reason for normalization was to exclude the effect of altitude variation on density. The normalization density $\rho_{\rm Obs}(\bar{h})$ can be obtained by formulating

$$\rho_{\rm Obs}(\bar{h}) = \rho_{\rm Obs}(h)\times\rho_{\rm MSIS}(\bar{h})/\rho_{\rm MSIS}(h),$$

where $\bar{h}$ denotes the mean altitude, $\rho_{\rm Obs}(h)$ is the direct observation along the satellite orbit, and correspondingly, $\rho_{\rm MSIS}(\bar{h})$ and $\rho_{\rm MSIS}(h)$ are the NRLMSISE00 model values. This method is widely used in the scientific study of thermospheric mass density (Picone et al.,

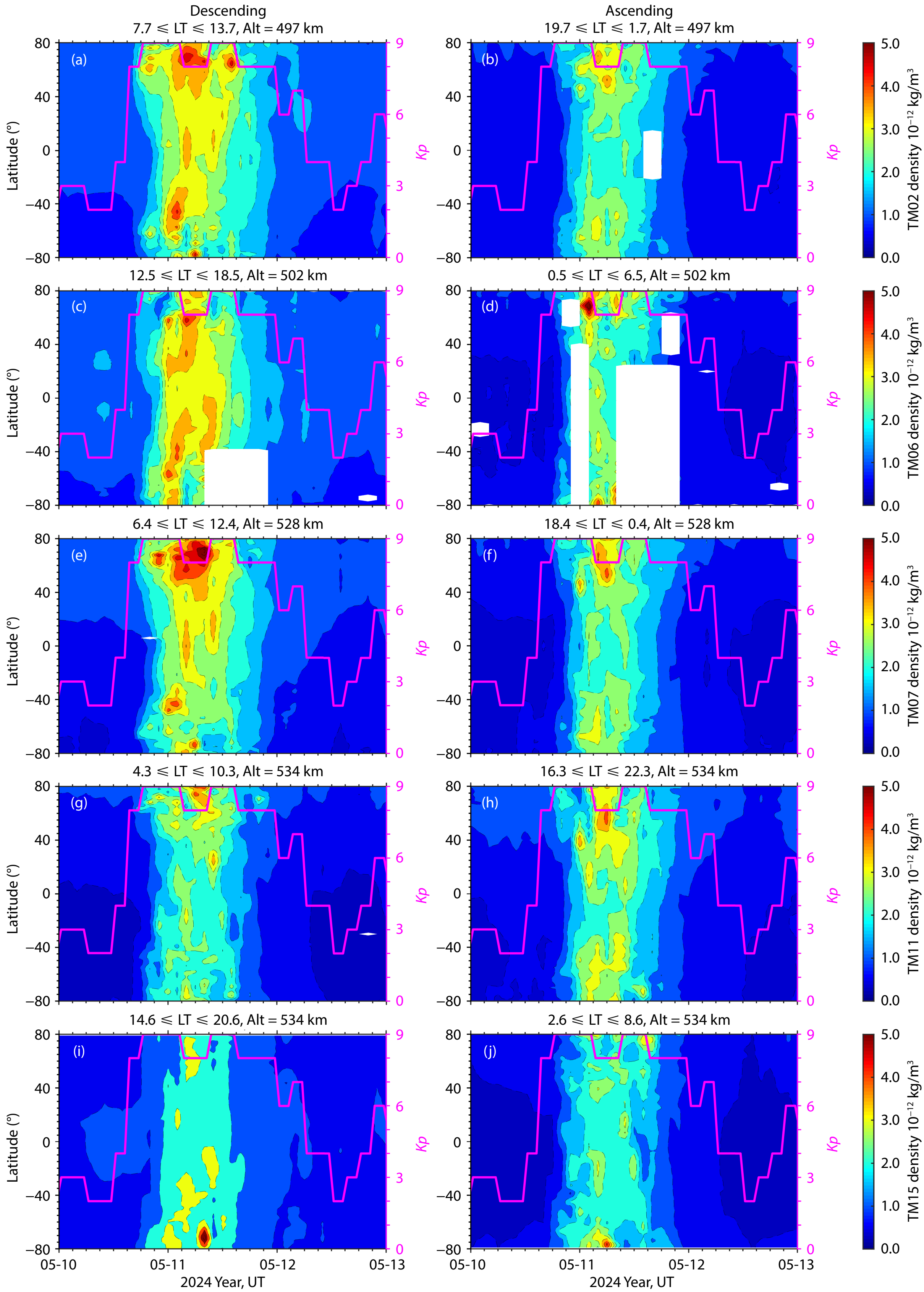

Figure 3. Thermosphere mass density responses during the strong geomagnetic disturbance on May 10–12, 2024. The left and right columns show the results of the corresponding satellite's descending and ascending orbits, respectively, and the densities are normalized to the corresponding average altitude. From top to bottom, the observations of satellites TM02, TM06, TM07, TM11, and TM15. The ocean red line above each panel represents the geomagnetic index *Kp*.

2002; Bruinsma et al., 2006). Because the perigee and apogee of the TianMu-1 satellites selected in this work are approximately 30 km apart and the average altitude is normalized to less than one scale height, the error caused by this method is small.

Because of the distinct LTs associated with satellite descending and ascending orbits, Figure 3 presents all satellite results categorized by descending orbits (left column) and ascending orbits (right column). Figure 3a displays the mass density variations with universal time (UT) and latitude observed during the TM02 descending orbit (prenoon sector, ~10.7 LT). Atmospheric disturbances of varying spatial scales are evident in the mid- to high-latitude regions of the northern hemisphere. At 19:30 UT on May 10, a TAD structure with an amplitude of approximately 3.89×10^{-12} kg/m^3 at hundred-kilometer scale was detected near 70°N. As geomagnetic activity intensified, the density amplitude increased to 4.78×10^{-12} kg/m^3, and the spatial extent of the disturbance expanded to thousand-kilometer scale. As the magnetic storm entered the recovery phase, the scale of the density disturbance in the high-latitude region recovered to a level marginally higher than that observed prior to the storm. Similar multiscale atmospheric density disturbances during the storm were also observed in the southern hemisphere. Comparative analysis of the initial disturbance onset times in the polar regions from TM02 revealed that the enhancement occurred earlier in the northern hemisphere than in the southern hemisphere. Approximately 3 hours later, distinct disturbances appeared in the mass density near the equator. This time lag corresponds to the propagation duration required for TADs to reach the equator, thus allowing the inference of a TAD propagation speed on the order of hundreds of meters per second. This result is consistent with the findings reported by Bruinsma and Forbes (2007).

Figure 3b displays the mass density observations from the TM02 satellite during its ascending orbit (~22.7 LT). Similar to the descending orbit observations, TADs of varying intensities are present in the mid- to high-latitude regions. The ascending orbit data also reveal higher density values in the northern hemisphere, consistent with the pattern observed in the descending orbit data. During the main phase of the magnetic storm, the density in the high-latitude northern hemisphere increased to 4.01×10^{-12} kg/m^3, exceeding the value of 3.37×10^{-12} kg/m^3 observed around 60°S in the southern hemisphere. Unlike the descending orbit period, however, the ascending orbit observations reveal that density disturbances in the polar regions exhibit no significant temporal difference in their response to the magnetic storm and that the propagation delay of atmospheric density disturbances to low-latitude and equatorial regions is notably shorter.

Figures 3c and 3d present the mass density observations from the TM06 satellite during its descending and ascending orbits, respectively. Blank areas in the plots result from satellite attitude adjustments, which prevent the ADD from operating effectively in the free molecular flow. A comparison between Figures 3a and 3c reveals similarities in density variations between TM02 and TM06 during their descending phases, primarily manifested in temporal differences in the polar disturbance onset and propagation characteristics of TADs toward low-latitude and equatorial regions. However, two significant differences emerge: (1) A pronounced density trough appears at latitudes above 60°N approximately 3 hours before May 11; and (2) TM02 shows a minimal difference in the disturbance duration between high and low latitudes, whereas TM06 observes an approximately 3-hour longer disturbance persistence in the low-latitude region (~30°S–30°N) compared with high latitudes. Figure 3d demonstrates a substantial density enhancement near 70°N in the northern hemisphere, reaching a peak intensity of 5.86×10^{-12} kg/m^3. Despite partial data gaps in the low-latitude regions, multiscale TAD structures remain discernible.

Figures 3e and 3f present mass density observations from the TM07 satellite normalized to 528 km altitude during its descending orbit (~9.3 LT) and ascending orbit (~21.3 LT). Despite differences in orbital altitude and LT compared with TM02, both satellites exhibit fundamentally similar density variation patterns during the magnetic storm. Descending orbit measurements reveal maximum densities of 3.29×10^{-12} kg/m^3 (northern hemisphere) and 2.38×10^{-12} kg/m^3 (southern hemisphere). During the ascending orbit, peak densities reach 7.39×10^{-12} kg/m^3 near 55°N and 4.43×10^{-12} kg/m^3 in the southern hemisphere. Collectively, TM07 observations demonstrate consistently higher density values in the northern hemisphere than in the southern hemisphere across both orbital configurations.

As indicated in Table 1, the descending and ascending nodes of the TM11 satellite are positioned at 07:20 LT and 19:20 LT, respectively, with corresponding density observations presented in Figures 3g and 3h. The TM11 observations demonstrate characteristic propagation signatures of TADs. During the ascending orbit phase, a TAD with an amplitude of 3.88×10^{-12} kg/m^3 formed near 40°N in the northern hemisphere at 00:00 UT on May 11, followed by the development of TADs with an amplitude of 3.31×10^{-12} kg/m^3 near 55°S in the southern hemisphere at 01:30 UT. Approximately 3 hours later, these two TAD systems converged near the equatorial region and interacted, generating new TAD structures with a density of 2.85×10^{-12} kg/m^3. As the magnetic storm progressed, energy injection into the polar regions led to the formation of TADs exhibiting an amplitude of 4.18×10^{-12} kg/m^3 at 75°N in the northern hemisphere by 06:00 UT. When propagating to 30°N, the amplitude of these disturbances decreased to 3.15×10^{-12} kg/m^3. Subsequent convergence of northern and southern hemisphere TADs at ~8°S produced new disturbances with further reduced intensity (2.56×10^{-12} kg/m^3). The most intense TAD during the ascending orbit phase emerged near 74°N in the northern hemisphere and registered an amplitude of 3.52×10^{-12} kg/m^3.

Figures 3i and 3j present observations from the TM15 satellite during its dawn-side (ascending orbit) and dusk-side (descending orbit) phases. Two distinct differences emerge compared with density characteristics observed by other satellites. First, the descending orbit of TM15 reveals atmospheric density disturbances occurring approximately 3 hours earlier in the high-latitude southern hemisphere than in the northern hemisphere—in contrast with other satellites' observations, where northern hemisphere perturbations typically precede southern hemisphere disturbances. Second, both descending and ascending orbit data from TM15 indicate stronger absolute densities in the southern hemisphere than the northern hemisphere during the magnetic storm. Additionally, dusk-side observations exhibit larger spatial scales and TADs of greater intensity in the southern hemisphere compared with the dawn side, exemplified by TADs near 73°S reaching an intensity of 6.27×10^{-12} kg/m^3 and spatial scales approximating the thousand-kilometer level.

3.2 Hemispheric Asymmetry

Although numerous studies have investigated hemispheric asymmetries in the thermospheric density response during geomagnetic storms (Bruinsma et al., 2006; Ercha et al., 2012; Zhu QY et al., 2023), their reliance on single-satellite observations inherently limits simultaneous multi-LT coverage. In contrast, our analysis of hemispheric asymmetry leverages coordinated multisatellite observations from a constellation, enabling concurrent acquisition of global density data across multiple LT sectors during storms. This approach provides systematic observational evidence essential for elucidating the full spatiotemporal characteristics of asymmetry. Figure 3 shows the variation in absolute density, but also noted are differences in the density of the northern and southern hemispheres of different satellites during the quiet period owing to the influence of different LTs. For example, the density of the southern hemisphere is higher than that of the northern hemisphere of TM07, whereas the density of the northern and southern hemispheres of TM15 is symmetrical with respect to the equator in the middle and low latitudes. Therefore, it is necessary to calculate the difference in the density of the relative quiet period to analyze the quantitative impact of magnetic storms on the thermospheric atmosphere. The quantitative calculation method is $(\rho/\rho_{\text{quiet}} - 1) \times 100\%$, where ρ_{quiet} is the density average value of May 9, and the results are shown in Figure 4. The color scale is consistent to facilitate comparison between different satellites.

As is evident from Figure 4, observations across all satellites—regardless of whether for ascending or descending orbits—demonstrate higher relative density differences in the southern hemisphere compared with the northern hemisphere, revealing hemispheric asymmetry in the thermospheric mass density response during disturbance periods. Furthermore, with the exception of TM11, all satellites exhibit substantially greater density enhancements and expanded disturbance regions during ascending orbits relative to descending orbits. During ascending passes, the four satellites (TM02, TM06, TM07, TM15) exhibit global-scale atmospheric perturbations, whereas during descending passes they show smaller enhancements primarily confined to the southern hemisphere. In contrast, TM11 displays a similar latitudinal extent of atmospheric density perturbations between its ascending and descending passes. For TM02 and TM06, which share comparable orbital altitudes, the maximum density differences between ascending and descending orbits reach 560% and 760%, respectively, indicating quantifiable LT-dependent variations in thermospheric density perturbations.

Building on the preceding analysis, intense geomagnetic storms trigger substantial energy and momentum transfer from the magnetosphere to the thermosphere, causing initial atmospheric density enhancements in the polar regions. To quantify hemispheric asymmetries and their LT dependence, Figure 5 presents density enhancement ratios in the polar zones. Within each subpanel, the red and gray dots denote the average percentage density differences within 60°N–90°N and 60°S–90°S, respectively, whereas the yellow bars represent the difference between southern and northern hemisphere mean values. During geomagnetically quiet periods, the hemispheric differences are negligible. Commencing with the storm onset at 17:00 UT on May 10, atmospheric density enhancements become markedly higher in the southern hemisphere relative to the northern hemisphere, with this hemispheric disparity gradually intensifying as the storm progresses. Observations from all satellites consistently demonstrate greater polar density enhancements in the southern hemisphere. During this event, maximum south–north differences reach 195% (TM02), 300% (TM06), 460% (TM07), 640% (TM11), and 435% (TM15). These results indicate that hemispheric asymmetries in storm-time density enhancements are modulated by both altitude and LT. Additionally, during the storm recovery phase, hemispheric differences progressively diminish yet remain elevated above prestorm quiet-time levels.

3.3 Wave-like Structure

Figure 6 displays the latitude-dependent percentage density difference observed by TM02, TM06, TM07, TM11, and TM15 during the main phase of the geomagnetic storm (18:00 UT on May 10 to 16:00 UT on May 11), illustrating the latitudinal propagation of TADs. The left and right columns of Figure 6 correspond to descending and ascending orbits, respectively. In each subplot, lines of the same color represent observations from different satellites within the same time grid. For example, the dark blue lines denote 18:00 UT on May 10, and the deep red lines correspond to 16:00 UT on May 11. The color gradient, indicating temporal evolution, is consistent with the color scale sequence in Figure 3, with a 2-hour interval between adjacent color-coded curves. Taking the descending pass observations of TM02 (Figure 6a) as an example, we analyze the evolution of storm-driven TADs: During the initial main phase, the dark blue curve reveals enhanced density perturbations above 60° latitude in both hemispheres while equatorial regions remain largely undisturbed. As the storm progresses with continuous energy deposition into high latitudes, polar disturbances intensify substantially. Concurrently, density perturbations in the low to mid latitudes amplify by 100%–300%, as evidenced by the green and yellow curves showing large-scale TADs (>1000 km) emerging at the equator. Notably, for TM02, TM06, TM07, and TM15, TAD amplitudes during ascending passes systematically exceed those during descending passes. In contrast, TM11 observations exhibit minimal latitudinal amplitude differences between ascending and descending passes. The TianMu-1 constellation—comprising 12 satellites across diverse orbital planes—enables synchronous multi-LT global atmospheric density observations, providing the pivotal capability of investigating magnetosphere–ionosphere–thermosphere coupling dynamics during geomagnetic storms.

4. Discussion

As indicated in Section 3.2, all five satellites of the TianMu-1 constellation, distributed across multiple LTs globally, observed a

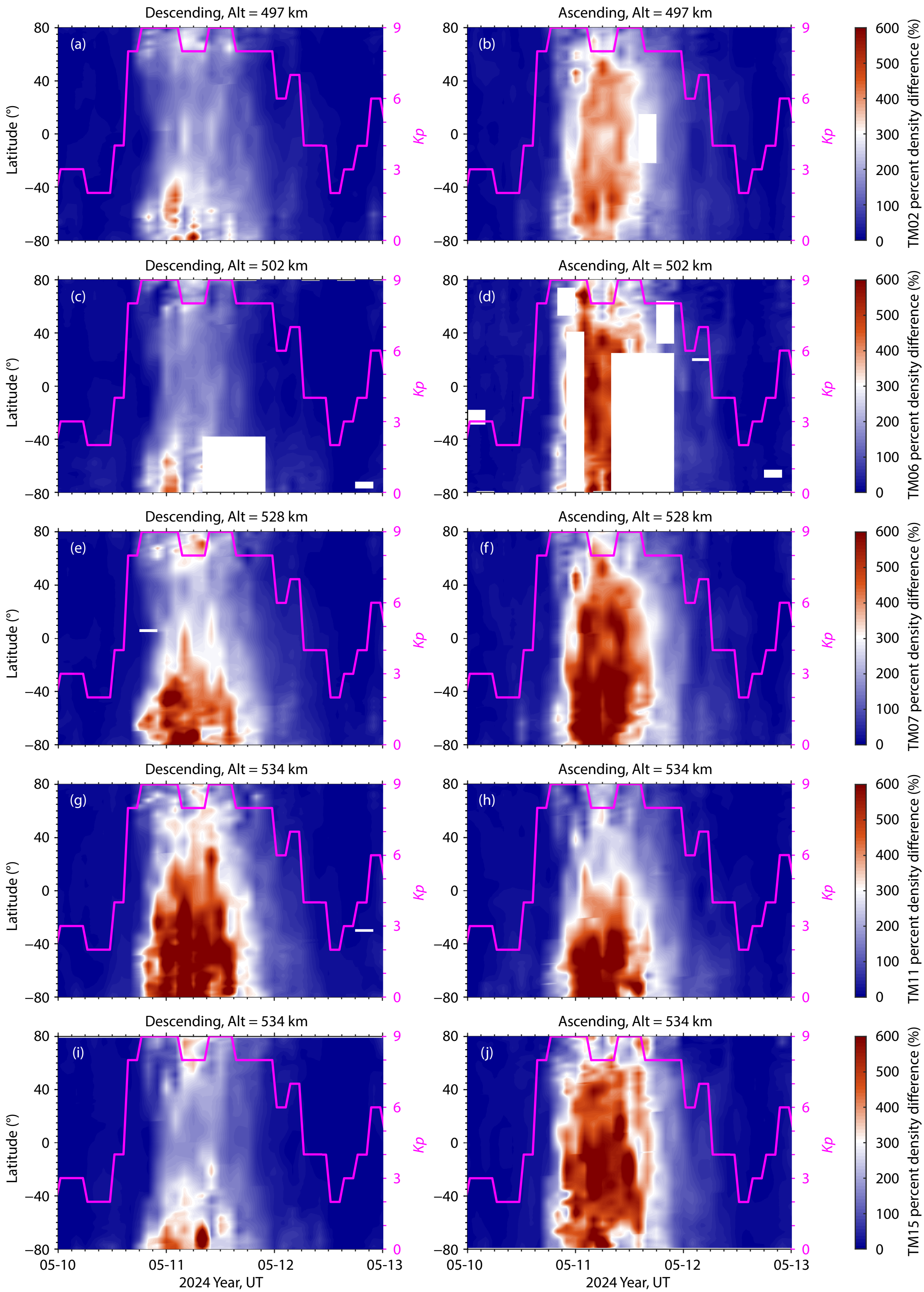

Figure 4. Same as Figure 3, except that the percentage density difference is presented. The color scale is the same for all panels.

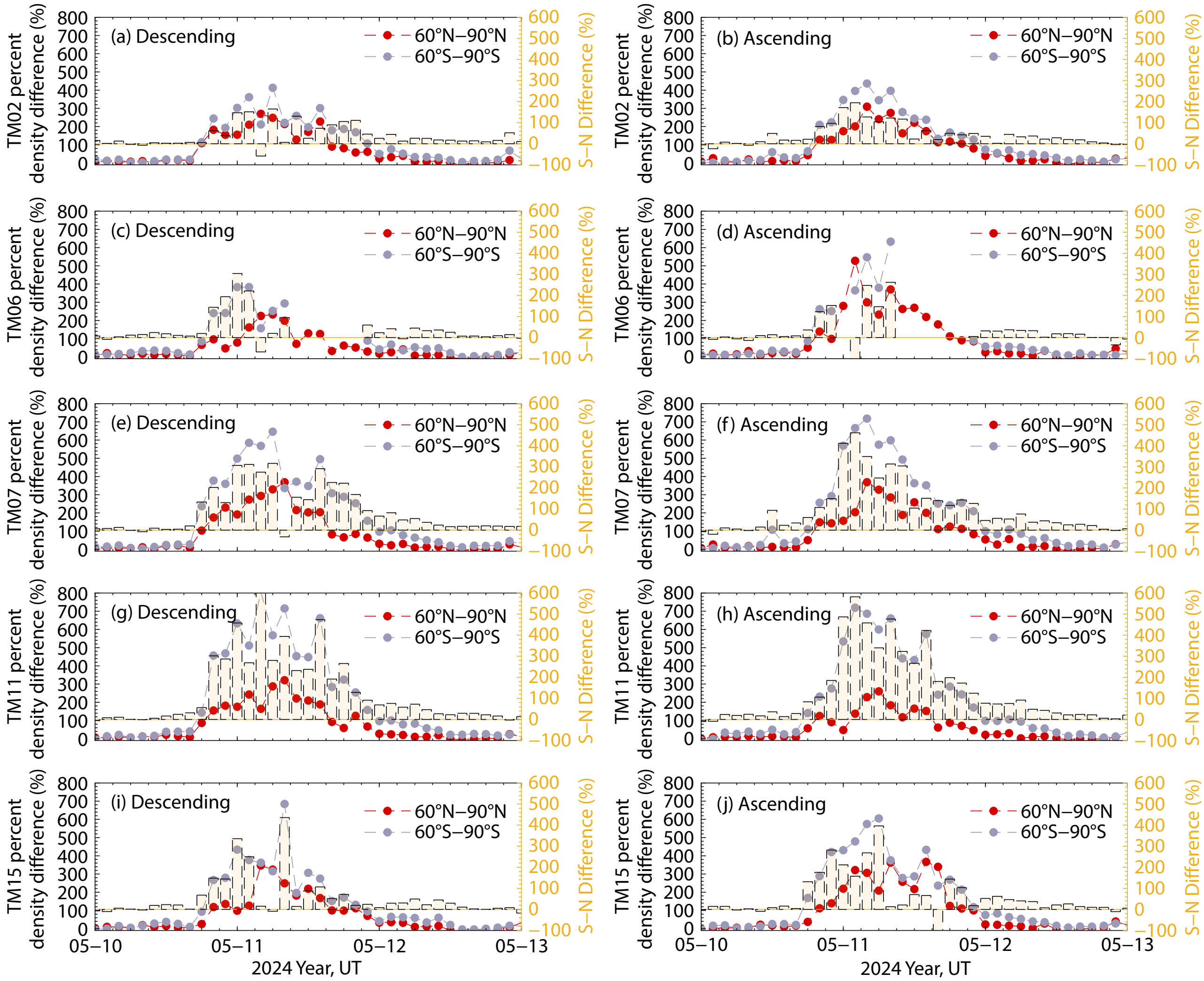

Figure 5. Density difference curve from May 10 to 12, 2024. The red dots and gray dots represent the mean percentages of 60°N–90°N and 60°S–90°S, respectively. From top to bottom, TM02, TM06, TM07, TM11, and TM15 results. The left and right columns are on descending and ascending orbits, respectively. The histogram for each panel represents the differences between the southern and northern hemispheres.

larger amplitude enhancement of mass density in the southern hemisphere compared with that in the northern hemisphere. Regarding the mechanism behind the hemispheric asymmetry in the response during storm time, several related prior studies have offered explanations. For instance, by analyzing plasma drift data from the Defense Meteorological Satellite Program (DMSP) F15 spacecraft, Ercha et al. (2012) found stronger plasma drift in the southern hemisphere ionosphere than in the northern hemisphere. This observation is consistent with measurements showing a higher thermospheric mass density response in the southern hemisphere during geomagnetic storms. Similarly, for the intense geomagnetic storm event in May 2024 studied in this work, we analyzed the global north–south differences by combining plasma convection data observed by the global Super Dual Auroral Radar Network (SuperDARN). The SuperDARN comprises an international array of ground-based high-frequency radars, including six radars in China (Zhang JJ et al., 2024). This network acquires line-of-sight (LOS) measurements of plasma drift velocities across mid- to high-latitude ionospheric regions. For the present analysis, we utilize statistically fitted plasma convection velocities derived through the following computational procedure: First, raw LOS velocity measurements undergo spatiotemporal smoothing via filtering applied to clustered adjacent beams, range gates, and sequential sweeps. The processed velocities are then mapped onto a regular grid in geomagnetic coordinates (magnetic latitude/magnetic local time [MLAT/MLT]) through sorting and interpolation. Finally, the gridded velocity field is assimilated into an established statistical convection model to generate the fitted velocity solutions (Ruohoniemi and Baker, 1998).

Figure 7 displays convection patterns derived from SuperDARN observations during the main phase of the storm (02:38–02:40 UT on May 11). The Thomas–Shepherd 2018 (TS18) empirical model (Thomas and Shepherd, 2018) provides the background electric potential distribution, with the convection pattern fitted by using an eighth-order spherical harmonic expansion. Cross-polar cap potential (Φ_{PC}) and gridded LOS velocity data coverage (N) are annotated for both the (a) northern and (b) southern hemispheres. In each panel, the solid black line demarcates the edge of the convection zone, where the electrostatic potential is defined as zero (Heppner and Maynard, 1987).

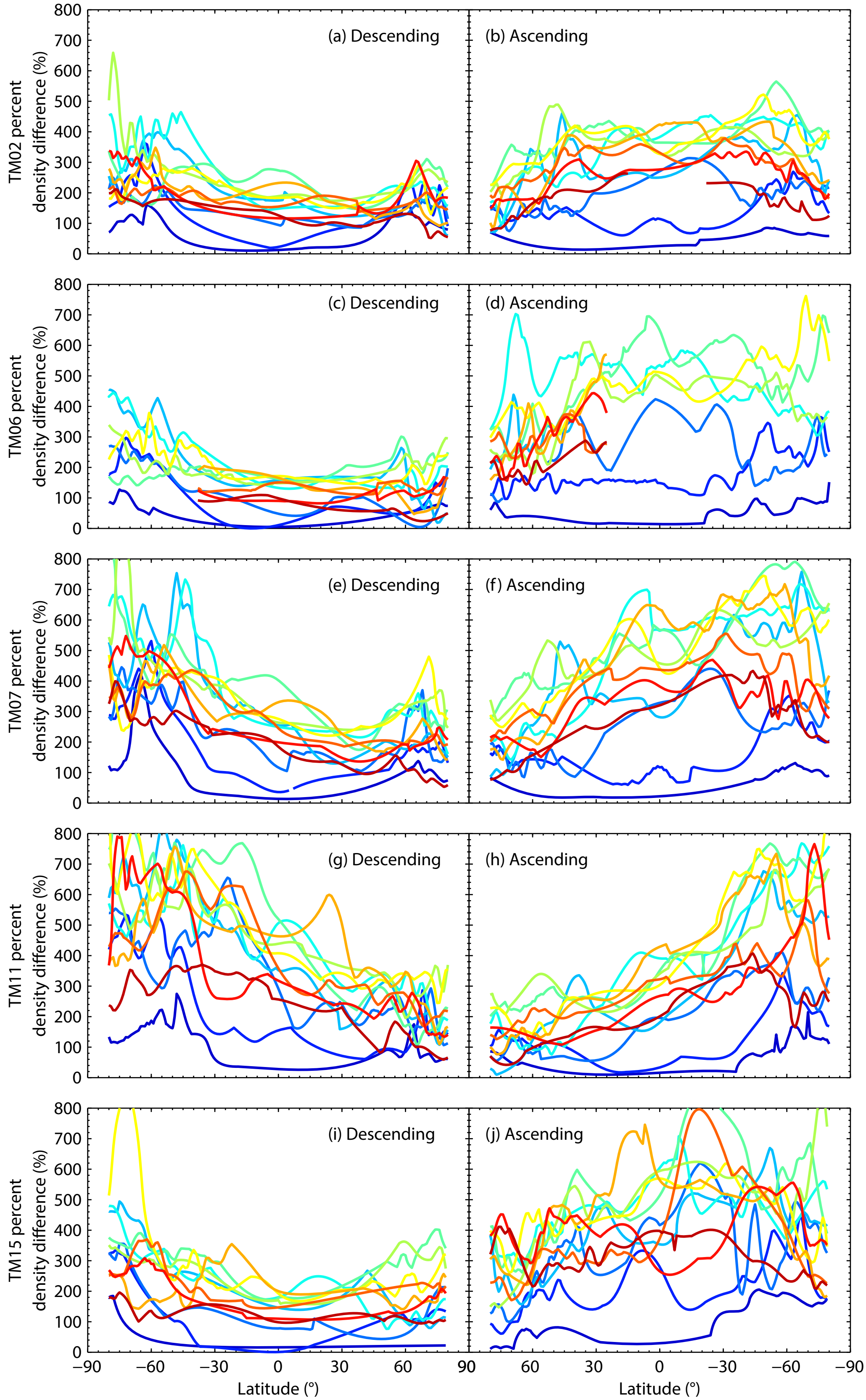

Figure 6. Percentage density differences from TM02, TM06, TM07, TM11, and TM15 as a function of latitude. The time range of the colored lines is from 18:00 UT on May 10 to 16:00 UT on May 11, with a time interval of 2 hours, and the color evolution (from dark blue to dark red) is consistent with the order of the color scale from small to large in Figure 3.

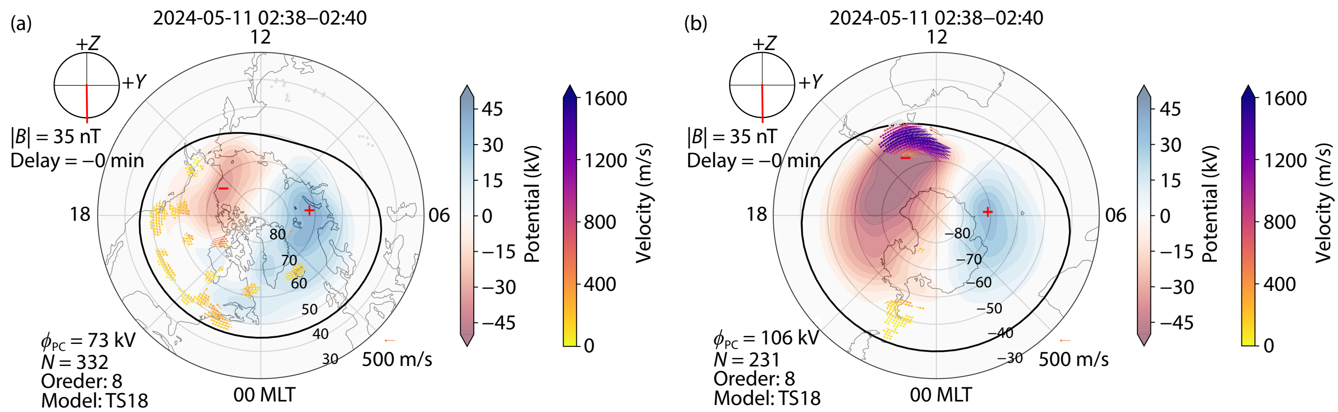

Figure 7. Convection pattern derived from SuperDARN observations (including six radars in China). Panels (a) and (b) display northern and southern hemisphere convection maps from 02:38 to 02:40 UT on May 11 (main phase of the storm), plotted in magnetic latitude versus magnetic local time coordinates. The Thomas–Shepherd 2018 (TS18) model provides the background electric potential distribution (intensity scaled by the first color bar). The magnitude of the fitted convection velocity vectors is represented by both vector length and the color in the second color bar.

As depicted in Figures 7a and 7b, during the geomagnetic storm interval (17:04–17:06 UT), the zero-potential contour expands equatorward to approximately 40° MLAT in both hemispheres. The Φ_{PC} reaches 106 kV in the southern hemisphere and 73 kV in the northern hemisphere. Convection velocities reach up to 1600 m/s near 60° MLAT postnoon of the southern hemisphere, whereas northern hemisphere velocities remain predominantly within 100 m/s. These results demonstrate substantially stronger ionospheric convection in the southern hemisphere. Such substantial north–south convection differences likely led to distinct levels of ion-neutral frictional heating between the hemispheres, which in turn contributed to the higher thermospheric density response amplitude in the southern hemisphere than in the northern hemisphere.

5. Summary

In this study, we used the TM02, TM06, TM07, TM11, and TM15 satellite observations of the TianMu-1 constellation to analyze the response of the severe geomagnetic storm to the atmospheric density of the thermosphere in May 2024. The five satellites fly over different orbital planes and at slightly different altitudes. The main results of the analysis are as follows:

(1) The thermospheric atmosphere at high latitudes forms wave-like structures of different intensities and spatial scales under the disturbance of strong magnetic storms, and these wave-like structures can propagate to the equatorial region. Descending orbit observations of TM02 revealed a TAD developing along the latitudinal direction at 19:30 UT on May 10, with an initial amplitude of ~3.89×10^{-12} kg/m^3 at hundred-kilometer scale. As geomagnetic activity intensified, the storm-enhanced density increased to 4.78×10^{-12} kg/m^3 while the disturbance expanded to thousand-kilometer scale. Approximately 3 hours after the onset of polar density disturbances, the equatorial mass density began increasing. This time lag corresponds to the propagation duration of TADs from the polar to equatorial regions.

(2) The atmospheric density of the thermosphere shows hemispheric response differences during magnetic storms. For absolute density, observations from four satellites (excluding TM15) showed higher densities in the northern hemisphere compared with the southern hemisphere. However, regarding the magnitude of perturbations in the relative density difference (expressed as a percentage), all satellites observed greater enhancements in the southern hemisphere than in the northern hemisphere. In this event, the maximum north–south differences observed above 60° latitude by the TM02, TM06, TM07, TM11, and TM15 satellites reached 195%, 300%, 460%, 640%, and 435%, respectively. Combined with SuperDARN observations, this pronounced hemispheric asymmetry may arise from differences in plasma convection patterns between the hemispheres.

(3) Atmospheric density perturbations show distinct LT differences during magnetic storms. For the TM02 descending orbit (~10.7 LT), the high-latitude perturbation onset occurred earlier in the northern hemisphere. Conversely, TM15 descending orbit (~17.6 LT) observations indicated that the southern hemisphere onset occurred ~3 hours earlier than that in the northern hemisphere. Furthermore, most satellites (TM02, TM06, TM07, TM15) exhibited larger density enhancements and a greater global spatial extent during the ascending orbit, whereas descending passes showed smaller enhancements primarily confined to the southern hemisphere. In contrast, TM11 displayed similar enhancement magnitudes and a similar spatial extent between its ascending and descending orbits.

Acknowledgments

We thank the National Space Science Center (NSSC) of the Chinese Academy of Sciences for full support of this research work. We are grateful to the team members who built the TianMu-1 constellation, as well as to Aerospace Tianmu (Chongqing) Satellite Technology Co., Ltd., for their support. This study was funded by the TianMu-1 Constellation Atmospheric Density Detector (Grant No. E3C1162110). The mass density data used in this article are available from the website https://www.tmsats.com/.

References

Ai, J. Z., Li, Y. P., Zhang, X. G., Xiao, C., Chen, G. M., Zheng, X. L., and Zhang, Z. L.

(2023). Study on the hemispheric asymmetry of thermospheric density based on in-situ measurements from APOD satellite. *Atmosphere*, *14*(4), 714. https://doi.org/10.3390/atmos14040714

Bruinsma, S., Forbes, J. M., Nerem, R. S., and Zhang, X. L. (2006). Thermosphere density response to the 20–21 November 2003 solar and geomagnetic storm from CHAMP and GRACE accelerometer data. *J. Geophys. Res.: Space Phys.*, *111*(A6), A06303. https://doi.org/10.1029/2005JA011284

Bruinsma, S. L., and Forbes, J. M. (2007). Global observation of traveling atmospheric disturbances (TADs) in the thermosphere. *Geophys. Res. Lett.*, *34*(14), L14103. https://doi.org/10.1029/2007GL030243

Bruinsma, S. L., and Forbes, J. M. (2009). Properties of traveling atmospheric disturbances (TADs) inferred from CHAMP accelerometer observations. *Adv. Space Res.*, *43*(3), 369–376. https://doi.org/10.1016/j.asr.2008.10.031

Cai, L., Aikio, A. T., and Nygrén, T. (2014). Solar wind effect on Joule heating in the high-latitude ionosphere. *J. Geophys. Res.: Space Phys.*, *119*(12), 10440–10455. https://doi.org/10.1002/2014JA020269

Cai, X. G., Wang, W. B., Lin, D., Eastes, R. W., Qian, L. Y., Zhu, Q. Y., Correira, J., McClintock, W. E., Gan, Q., … Karan, D. K. (2023). Investigation of the Southern Hemisphere mid-high latitude thermospheric $\sum O/N_2$ responses to the Space-X storm. *J. Geophys. Res.: Space Phys.*, *128*(3), e2022JA031002. https://doi.org/10.1029/2022JA031002

Chernogor, L. F., Rozumenko, V. T., Shevelev, M. B., Wang, J., and Zheng, Y. (2025). Global geomagnetic response to the extreme geospace storm of May 10–11, 2024. *Adv. Space Res.*, *76*(2), 939–967. https://doi.org/10.1016/j.asr.2025.05.004

Cnossen, I., Emmert, J. T., Garcia, R. R., Elias, A. G., Mlynczak, M. G., and Zhang, S. R. (2024). A review of global long-term changes in the mesosphere, thermosphere and ionosphere: A starting point for inclusion in (semi-) empirical models. *Adv. Space Res.*, *74*(11), 5991–6011. https://doi.org/10.1016/j.asr.2024.10.005

Denton, M. H., Borovsky, J. E., Skoug, R. M., Thomsen, M. F., Lavraud, B., Henderson, M. G., McPherron, R. L., Zhang, J. C., and Liemohn, M. W. (2006). Geomagnetic storms driven by ICME- and CIR-dominated solar wind. *J. Geophys. Res.: Space Phys.*, *111*(A7), A07S07. https://doi.org/10.1029/2005JA011436

Emmert, J. T., Lean, J. L., and Picone, J. M. (2010). COSPAR international reference atmosphere: 2007. *Adv. Space Res.*, *45*(10), 1072–1092.

England, S. L., Greer, K. R., Zhang, S. R., Evans, S., Solomon, S. C., Eastes, R. W., McClintock, W. E., and Burns, A. G. (2021). First comparison of traveling atmospheric disturbances observed in the middle thermosphere by Global-scale Observations of the Limb and Disk to traveling ionospheric disturbances seen in ground-based total electron content observations. *J. Geophys. Res.: Space Phys.*, *126*(6), e2021JA029248. https://doi.org/10.1029/2021JA029248

Ercha, A., Ridley, A. J., Zhang, D. H., and Xiao, Z. (2012). Analyzing the hemispheric asymmetry in the thermospheric density response to geomagnetic storms. *J. Geophys. Res.: Space Phys.*, *117*(A8), A08317. https://doi.org/10.1029/2011JA017259

Fujiwara, H., and Miyoshi, Y. (2006). Characteristics of the large-scale traveling atmospheric disturbances during geomagnetically quiet and disturbed periods simulated by a whole atmosphere general circulation model. *Geophys. Res. Lett.*, *33*(20), L20108. https://doi.org/10.1029/2006GL027103

Heppner, J. P., and Maynard, N. C. (1987). Empirical high - latitude electric field models. *J. Geophys. Res.: Space Phys.*, *92*(A5), 4467–4489. https://doi.org/10.1029/ja092ia05p04467

Li, R. X., and Lei, J. H. (2021). Responses of thermospheric mass densities to the October 2016 and September 2017 geomagnetic storms revealed from multiple satellite observations. *J. Geophys. Res.: Space Phys.*, *126*(1), e2020JA028534. https://doi.org/10.1029/2020JA028534

Li, X., Xu, J. Y., Tang, G. S., Chen, G. M., Man, H. J., Liu, S. S., and Li, Y. P. (2018). Processing and calibrating of in-situ atmospheric densities for APOD. *Chin. J. Geophys. (in Chinese)*, *61*(9), 3567–3576. https://doi.org/10.6038/cjg2018L0452

Li, Y. P., Sun, Y. Q., Zhang, X. G., Du, Q. F., Tang, X. C., Zheng, X. L., Ai, J. Z., Meng, X. G., Li, J., … Wei, S. L. (2023). The preliminary result of orbital atmosphere detector on board spherical satellite. *Sci. Sin. Technol. (in Chinese)*, *53*(4), 615–621. https://doi.org/10.1360/SST-2022-0074

Li, Y. P., Sun, Y. Q., Zhang, X. G., Ai, J. Z., Zheng, X. L., Li, J., Wang, Y. J., Guo, B. B., Yan, F., … Cao, Y. Y. (2024). Thermosphere joint observations by TM-1 constellations and Swarm-B during the April 2023 geomagnetic storm. *Earth Planet. Phys.*, *8*(2), 307–316. https://doi.org/10.26464/epp2024002

Liu, H., Lühr, H., and Ma, S. (2014). Global structure and temporal evolution of the thermosphere density response to geomagnetic storms. *J. Geophys. Res.: Space Phys.*, *119*(4), 2829–2844.

Pham, K. H., Zhang, B., Sorathia, K., Dang, T., Wang, W., Merkin, V., Liu, H., Lin, D., Wiltberger, M., … Lyon, A. M. (2022). Thermospheric density perturbations produced by traveling atmospheric disturbances during August 2005 storm. *J. Geophys. Res.: Space Phys.*, *127*(2), e2021JA030071. https://doi.org/10.1029/2021JA030071

Picone, J. M., Hedin, A. E., Drob, D. P., and Aikin, A. C. (2002). NRLMSISE-00 empirical model of the atmosphere: Statistical comparisons and scientific issues. *J. Geophys. Res.: Space Phys.*, *107*(A12), 1468. https://doi.org/10.1029/2002JA009430

Powell, J. (2018). Atmospheric factors and features. In J. Powell (Ed.), *Rare Astronomical Sights and Sounds*. Cham: Springer. https://doi.org/10.1007/978-3-319-97701-0_8

Qin, G. T., Xu, G. L., and Ma, Z. H. (1990). Measurements of neutral atmospheric density using ionization gauge. *Research of Space Physics (in Chinese)*, *5*(2), 143–149.

Richards, P. G., Pinnock, M., and La Hoz, C. (2013). Geomagnetic storms. *Space Sci. Rev.*, *178*(1-4), 3–18.

Ruohoniemi, J. M., and Baker, K. B. (1998). Large-scale imaging of high-latitude convection with Super Dual Auroral Radar Network HF radar observations. *J. Geophys. Res.: Space Phys.*, *103*(A9), 20797–20811. https://doi.org/10.1029/98JA01288

Sarris, T. E. (2019). Understanding the ionosphere thermosphere response to solar and magnetospheric drivers: Status, challenges and open issues. *Philos. Trans. Roy. Soc. A: Math., Phys. Eng. Sci.*, *377*(2148), 20180101. http://dx.doi.org/10.1098/rsta.2018.0101

Solomon, S. C., Qin, D., and Manning, M. (2007). Contribution of stratosphere-troposphere exchange to the chemistry of the troposphere and lower stratosphere. *Atmos. Chem. Phys.*, *7*(11), 2723–2748.

Thomas, E. G., and Shepherd, S. G. (2018). Statistical patterns of ionospheric convection derived from mid-latitude, high-latitude, and polar SuperDARN HF radar observations. *J. Geophys. Res.: Space Phys.*, *123*(4), 3196–3216. https://doi.org/10.1002/2018JA025280

Wang, X., Miao, J., Aa, E., Ren, T. L., Wang, Y. X., Liu, J., and Liu, S. Q. (2020). Statistical analysis of Joule heating and thermosphere response during geomagnetic storms of different magnitudes. *J. Geophys. Res.: Space Phys.*, *125*(8), e2020JA027966. https://doi.org/10.1029/2020JA027966

Xiao, C., He, F., Shi, Q. Q., Liu, W. L., Tian, A. M., Guo, R. L., Yue, C., Zhou, X. Z., Wei, Y., … Zhang, Z. (2023). Evidence for lunar tide effects in Earth's plasmasphere. *Nat. Phys.*, *19*(4), 486–491. https://doi.org/10.1038/s41567-022-01882-8

Xu, S., Vadas, S. L., and Yue, J. (2021). Thermospheric traveling atmospheric disturbances in austral winter from GOCE and CHAMP. *J. Geophys. Res.: Space Phys.*, *126*(9), e2021JA029335. https://doi.org/10.1029/2021JA029335

Zhang, B., Lotko, W., Brambles, O., Wiltberger, M., Wang, W., Schmitt, P., and Lyon, J. (2012). Enhancement of thermospheric mass density by soft electron precipitation. *Geophys. Res. Lett.*, *39*(20), L20102. https://doi.org/10.1029/2012GL053519

Zhang, J. J., Lan, A. L., Yan, J. Y., Deng, X., Wang, W., Li, H., Sun, L. C., Nan, Y., Song, X. C., and Wang, C. (2024). Development of the Chinese dual auroral radar network and preliminary results. *Space Wea.*, *22*(10), e2024SW004131. https://doi.org/10.1029/2024SW004131

Zhu, Q. Y., Lu, G., Lei, J. H., Deng, Y., Doornbos, E., van den IJssel, J., and Siemes, C. (2023). Interhemispheric asymmetry of the thermospheric neutral density response to the 7–9 September 2017 geomagnetic storms. *Geophys. Res. Lett.*, *50*(11), e2023GL103208. https://doi.org/10.1029/2023gl103208